Journal of the European Ceramic Society 19 (1999) 1967–1978

PII: S0955-2219(99)00016-3
0955-2219/99/$ - see front matter

Sintering of a Transition Alumina: Effects of Phase Transformation, Powder Characteristics and Thermal Cycle

C. Legros,[a] C. Carry,[b]* P. Bowen[c] and H. Hofmann[c]

[a]Laboratoire d'Etudes des Matériaux Hors Equilibre (LEMHE), Université de Paris-Sud, Bâtiment 410, 91405 Orsay Cedex, France
[b]LTPCM, UMR5614 CNRS-INPG/UJF, ENSEEG, B.P. 75, 38402 Saint Martin D'Heres Cedex, France
[c]Laboratoire de Technologie des Poudres, EPFL, MX D, CH 1015 Lausanne, Switzerland

(Received 21 October 1998; accepted 23 January 1999)

Abstract

The effects of several parameters on the pressureless sintering of a commercially available transition alumina has been investigated. The capacity of the particles to re-arrange during the phase transformation into the α-alumina phase has been shown to be a key feature in the densification mechanism. The degree to which the particle re-arrangement can lead to an enhanced densification over and above the change in density due to the phase transformation from γ to α phase depends on several parameters: compact density, heating rate and the amount of α-alumina present in the as-supplied raw powder. The parameters influencing the degree of particle re-arrangement and what directions to take to improve on the above densities and grain sizes are discussed. © *1999 Elsevier Science Limited. All rights reserved*

Keywords: phase transformation, sintering, microstructure: final, Al_2O_3, rearrangement.

1 Introduction

Most nanocrystalline oxide ceramic powders are metastable[1] and this metastability may have a critical influence on the sintering behaviour. Studies on producing nanocrystalline ceramics from fine powders (< 100 nm) have highlighted the problem of achieving high densities without excessive grain growth. It is particularly true for transition alumina powders which are currently produced with very high specific surface area and ultrafine crystallite sizes; the transformations into the stable α-alumina are generally accompanied by vermicular microstructures consisting of a network of large pores which develops during the transformation.[2,3] The final stages of sintering then require very high temperatures to achieve high densities. In recent literature on this subject, three main routes have been investigated to overcome this difficulty in elaborating dense nanograined alumina ceramics. The first, the α-alumina seeding of precursor gels (mostly boehmite) was explored and developed by Messing *et al.*;[4] it results[5,6] in the reduction of the transformation temperature and in a refinement of the final microstructure. Despite this breakthrough, whereupon gel fragments can be sintered to almost full density beyond about 1200°C, processing difficulties still seem to hinder its application to the production of monolithic pieces and that the mechanism remains to be elucidated.[7] The second approach consists of pressure sintering methods: uniaxial hot-pressing[8–10] or sinter-forging.[11] It has been suggested that during hot pressing of transition aluminas, pressure-induced particle rearrangement causes impingement of the growing α-alumina colonies,[2,3] thus limiting the formation of a vermicular pore microstructure. The last route involves the influence of doping elements on the γ to α transformation.[12–15] However in general no paper has reported an enhancement or retardation of the γ to α phase transformation of a sufficient magnitude to lead to a high-density nanograined monolithic material at sintering temperatures lower than those used for fine grained α-Al_2O_3 powders.

The ultimate goal of our study is the synthesis of α-Al_2O_3 nanoceramics starting from nanocrystalline γ-Al_2O_3, doped or undoped but without pressure

*To whom correspondence should be addressed.

assisted sintering. With the idea that a phase transformation could be used to enhance the densification of nanostructured alumina[16] and working on readily available commercial transition alumina powders, we explore the effects of various parameters on the densification behaviour. By following the densification curves and following the corresponding microstructural evolution we hope to elucidate the key mechanism of such phase transformation assisted densification. As illustrated in Fig. 1, the densification of γ-Al_2O_3 typically shows two regimes of densification during a constant heating rate experiment. The first, R1, is a rapid densification associated with the phase transition of γ-Al_2O_3 via the transition aluminas (δ and θ) to the stable α phase at around 1100°C, and the second, R2, a slower densification of the α-Al_2O_3 at higher temperatures. In this paper, we used commercial powders which differ mainly by their α-alumina contents; we vary the green densities by different cold isostatic pressing pressures and the thermal cycle mainly by varying heating rates. In a forthcoming second paper,[17] results concerning the effects of doping elements (magnesium, titanium, yttrium and zirconium) on the transformation-densification behavior of the same γ-alumina raw powder batch will be presented, analysed and discussed using a similar approach.

2 Powders and Experimental Procedures

All powders used in this work were provided by Baïkowski Chimie (France) and correspond to the Baïkalox CR125 commercial grade which is an alum derived γ-alumina. Characteristics of as-received powders are reported in Table 1. These four batches of CR125 powder differ mainly by their α-alumina contents which range from less than 0·5% for the Batch 1 (927 N) up to 6% for the Batch 4 (8966-4 Mg). Batches 3 and 4 correspond to CR125 γ-powders doped with magnesia at the alum stage and their α contents are rather high (4 and 6%, respectively); the α contents in these various powders has to be considered as an involuntary seeding. In fact these transition alumina powders are mainly composed of the θ crystalline phase which is the last metastable transition alumina with a cubic close packing of oxygen ions before the stable α-phase with hexagonal oxygen packing.[18] For reasons of simplicity we shall continue to describe the powder under its commercial description as γ-alumina. Transmission electron microscopy (TEM) observations show a primary particle size ranging from 15 to 20 nm. Specific surface areas were measured by nitrogen adsorption (BET model, ASAP 2010, Micromeritics, USA) on free powders and on powder compacts. The spherical primary particle diameter that can be calculated from the surface area d_{BET} was around 17 nm consistent with the TEM observations. These nanosized primary particles are strongly aggregated in the as-received powder and the aggregate sizes range from around 0·10 to 0·50 μm.

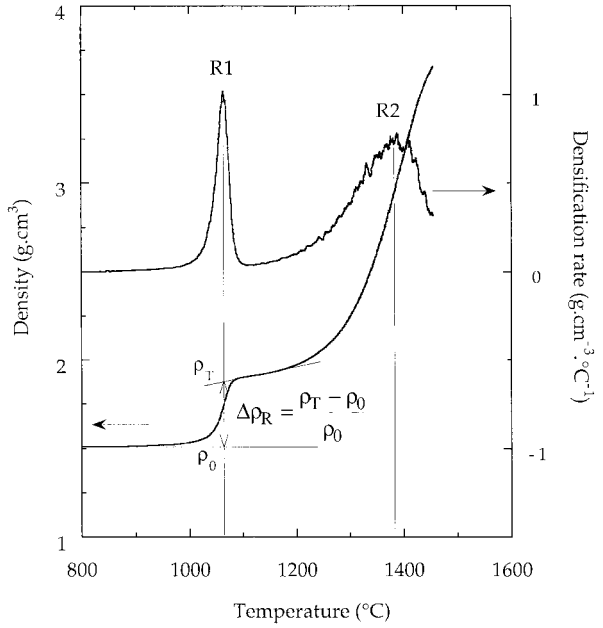

Fig. 1. Typical densification curves of transition alumina powder compact (batch 4, cold isostatic compaction pressure (CIP): 250 MPa, heating rate: 1°C min^{-1}).

Green compacts were produced by cold isostatic pressing (CIP) of the as-received powders; different CIP pressures from 75 up to 250 MPa were used and one sample was produced at 1 GPa from Batch 2. Cylindrical samples (diameters from 5 to 7 mm) were cold machined from these compacts with lengths from 6 to 10 mm depending on planed dilatometric experiments. The apparent shrinkage was followed by dilatometry (DI24 Adamel France with 2 mm maximum length variation or TMA 92 Setaram France with 4 mm maximum length variation and 2 g constant load on the sample). All samples were heated to 800°C at 10°C min^{-1} and thereafter to 1450°C under constant heating rate conditions: generally 1 or 10°C min^{-1} with some runs at 0·5, 5, 20 or 30°C min^{-1}. All densification and sintering treatments were performed in air. Densities, $\rho(T)$, and densification rate curves were computed from the recorded shrinkage data and from final density ρ_f measurements using the following formula:

$$\rho(T) = \left(\frac{1+\frac{\Delta L_f}{L_0}}{1+\frac{\Delta L(T)}{L_0}}\right)^3 \rho_f$$

in which L_0 is the initial sample length, L_f is the final sample length and $L(T)$ is the sample length at the temperature T. Final densities were mea-

Table 1. Characteristics of Baïkalox CR 125 commercial batches used for this work

Batch No.	*Commercial batch name*	*Specific area (BET) ($m^2 g^{-1}$)*	*α Content (%) (XRD)*	*MgO content (ppm wt)*	*Granulometry* D_{50} (μm)
1	927 N	110·0	< 0·5	—	0·31
2	8777	105·0	3·3	—	1·00
3	8965 (Mg)	95·3	4·0	500	0·31
4	8966 (4 Mg)	96·3	6·0	2000	0·64

sured by the classical Archimede's method on cooled samples.

Pore size distribution measurements were made using nitrogen isotherms (ASAP 2010, Micromeritics, USA, using the desorption curve and the BJH cylindrical model) on green samples. Also some samples cooled just after the first densification rate peak were characterized (R1 in Fig. 1) to monitor the porosity evolution during this first apparent densification step. With this method, the maximum pore size that can readily be measured is around 200 nm and therefore gives a pore volume fraction, V_{PF}, corresponding to pores < 200 nm. The Archimede's method measures the apparent density from which a total pore volume fraction, V_{PT}, can be deduced knowing the theoritical densities of considered crystalline phases (3.6 and 3.987 g cm^{-3} for, respectively, θ- and α-alumina phases). The relative difference between the fractional and total pore volume $V_{PR} = (V_{PF} - V_{PT}) / V_{PT}$ gives an estimation of the relative fraction of the pore volume not detected by nitrogen porosimetry, i.e. the fraction of pores with a diameter higher than 200 nm.

The phase transformations were investigated using X-ray powder diffraction (XRD). Microstructures and grain sizes were observed by scanning electron microscopy (SEM) on fractured surfaces.

3 Results

Figure 2 shows the densification behaviours (density and densification rate versus temperature) of Batch 1 and Batch 4 powders sintered at constant heating rates (1 and 10°C min^{-1}). These two batches represent the two extremes in α contents and the comparison of their densification behaviors with those of the other batches allows us to draw some general trends. In all cases, the temperature of first densification rate peak, R1, is lowered on decreasing the heating rate. For all heating rates, the R1 temperature decreases with increasing α content. In Fig. 2 the second densification rate peak, R2, appears only for the Batch 4 powder while for the Batch 1 powder this temperature is higher than 1450°C. The R2 temperature generally

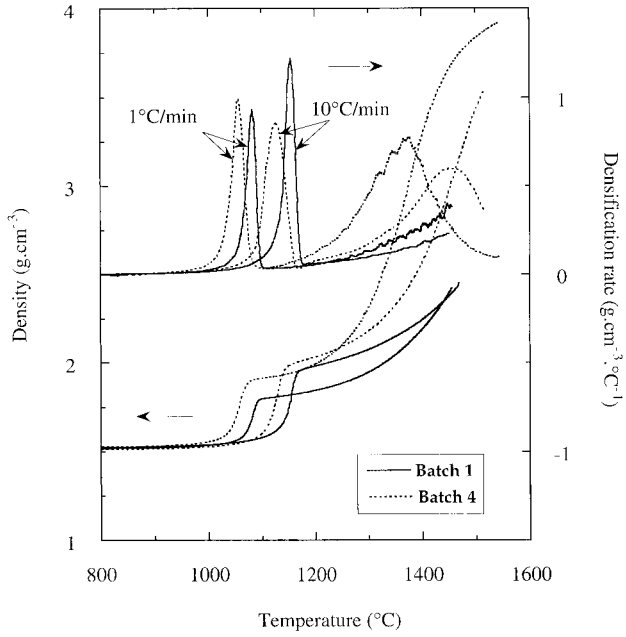

Fig. 2. Densification curves of batch 1 and 4 compacts (250 MPa CIP) with 1 and 10°C min^{-1} heating rates.

decreases with increasing α contents (Table 2). At the end of the first densification regime, XRD analysis reveals only α-alumina for all the powders. This means that this first densification step corresponds globally to the γ–α transformation. Significant differences in transformation relative density variation ($\Delta\rho_R$ as defined in Fig. 1) are observed and depend on powder batch and heating rate (Table 2).

Figure 3 illustrates, for Batch 1 powder compacts, the effect of the CIP pressure on the densification behavior of these transition alumina powders. As expected, the green density increases with increasing CIP pressure. For the same heating rate, the R1 temperature decreases when the CIP pressure is increased. It is interesting to note that the effect of the heating rates of 1 and 10°C min^{-1} on the relative density variation $\Delta\rho_R$ is enhanced as the green densities increase.

Figure 4 reports the densification curves (1°C min^{-1}) of compacts from three powders with different α contents but similar green densities: curves of Batch 3 are not reported for clarity but they agree with the general trends observed. This figure clearly shows that the R1 and R2 temperatures

Table 2. Densification characteristics

Batch no.	α *Content (%)*	T_{R1}[a] *(°C)*		$\Delta\rho_R$[b] *(%)*		T_{R2}[c] *(°C)*	
		1°C min^{-1}	*10°C min^{-1}*	*1°C min^{-1}*	*10°C min^{-1}*	*1°C min^{-1}*	*10°C min^{-1}*
1	< 0·5	1080	1156	16·5	24·0	N.D.[d] > 1450	N.D. > 1450
2	3·3	1065	1145	19·0	25·0	1435	1490
3	4·0	1063	1141	19·0	27·0	1395	N.D. > 1450
4	6·0	1058	1130	25·7	30·0	1375	1450

[a] T_{R1}, temperature of the first densification rate peak.
[b] $\Delta\rho_R$, transformation relative density variation, as defined in Fig. 1.
[c] T_{R2}, temperature of the second densification rate peak.
[d] N.D., not determined.

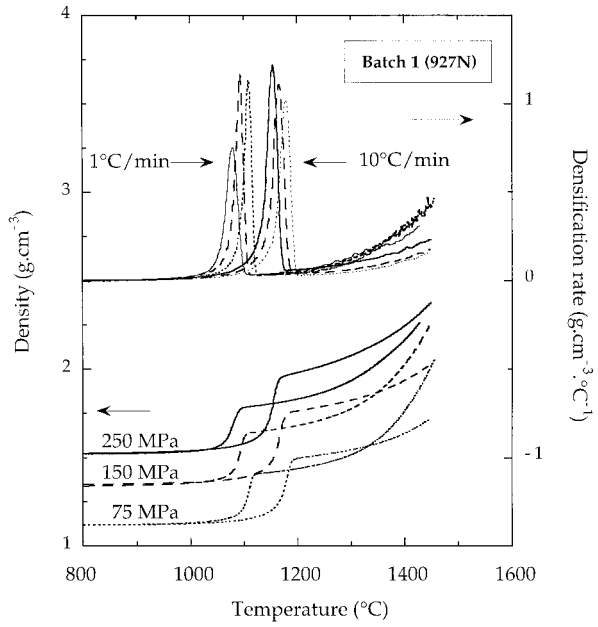

Fig. 3. Influence of the cold isostatic compaction pressure (CIP) on the densification curves of batch 1 for two different heating rates: 1 and 10°C min^{-1}.

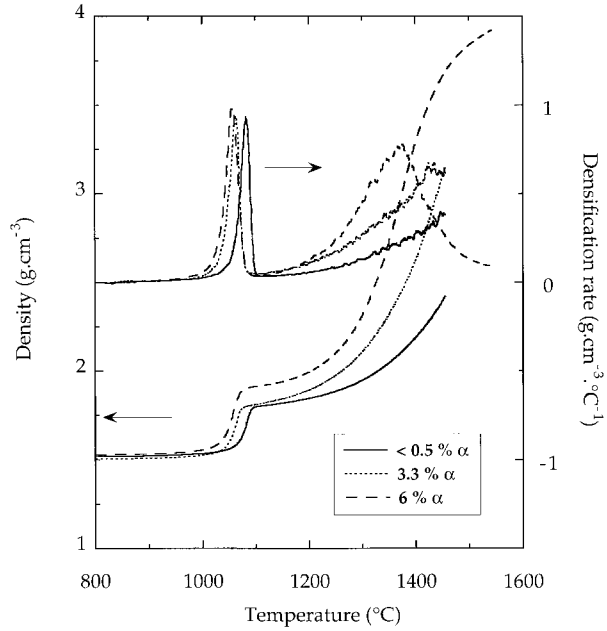

Fig. 4. Comparison of densification behaviours of powder with different α-alumina contents:250 MPa CIP and 1°C min^{-1} heating rate.

both decrease with increasing α content as has been previously observed by other authors.[4] The relative density variation $\Delta\rho_R$ is significantly higher for the highest α content; this difference is less pronounced for the 10°C/min^{-1} heating rate where all the powders exhibit nearly the same $\Delta\rho_R$.

Figure 5 shows the influence of the green density (varied via the CIP pressure) on the $\Delta\rho_R$ corresponding to the first densification step for all samples studied. It appears that the $\Delta\rho_R$ increases with a decrease in green density for all the powders and that for a given powder, the $\Delta\rho_R$ is systematically higher for the fastest heating rate. This influence of the heating rate is more visible in Fig. 6, where the ΔP_R is reported versus heating rate for the range 1–30°C min^{-1}.

Typical microstructures of sintered samples with constant heating rates (1 and 10°C min^{-1}) up to 1450°C are shown in Fig. 7. The Batch 1 samples exhibit vermicular microstructures; this is less pronounced in the case of 10°C min^{-1} heating rate. The grain size is higher for the lower heating rate (1°C min^{-1}); densities are rather low at about 2·35 g cm^{-3} hardly 60% of the theoritical α density. Sintered Batch 4 samples have cuboctahedral grains without marked vermicular microstructure and the density of the 1°C min^{-1} sample is near 90% of the theoretical density.

To investigate the microstructural evolution during the first densification step, dilatometric runs were interrupted at 1180°C and samples cooled at 10°C min^{-1}. As expected from densification curves (Fig. 2), only the Batch 1 sample heated at 1°C min^{-1} has a significantly lower density. For all the samples, only the α phase is detected by XRD. The corresponding microstructures observed by SEM are shown in Fig. 8. The green samples (250 MPa CIP pressure) seem to have a relatively homogeneous microstructure made up of particles or agglomerates with sizes ranging from 40 to 70 nm [Fig. 8(a)]. After heating up to 1180°C at 10°C min^{-1}, grains or particles appear regular in shape without the apparent substructure visible in the green compacts. Grain sizes are a little larger

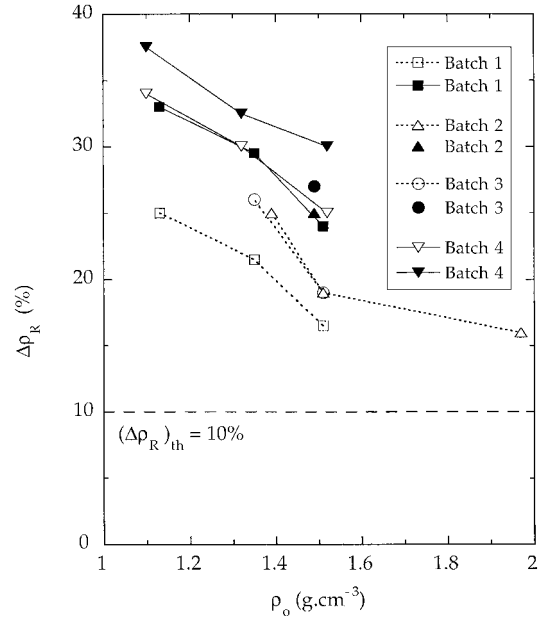

Fig. 5. Transformation relative density variation versus green density (CIP from 75 MPa up to 1 GPa) curves for the various powder batches and with two different heating rates (open symbols for 1°C min^{-1} and filled symbols for 10°C min^{-1}).

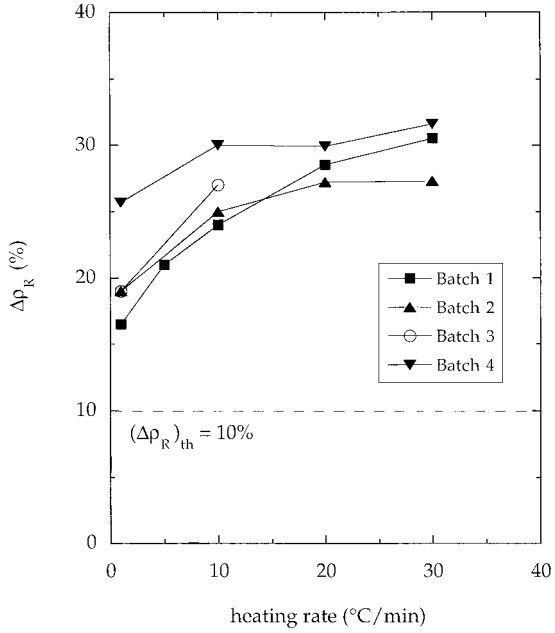

Fig. 6. Influence of the heating rate on the transformation relative density variation, $\Delta\rho_R$, for the various powder batches (250 MPa CIP).

for the Batch 1 sample (80–100 nm) than for the Batch 4 sample (70–80 nm). After heating up to 1180°C at 1°C min^{-1} a vermicular microstructure is visible for the Batch 1 sample while the grains in the Batch 4 sample are more or less cuboctahedric. Grain sizes are again larger in the Batch 1 sample (150 nm) than in the Batch 4 sample (100 nm).

The porosity of samples from interrupted dilatometric runs at 1180°C were investigated using nitrogen porosimetry and the pore size distributions are reported in Fig. 9(a) and (b) for Batch 1 and Batch 4, respectively. For green compacts (250 MPa CIP pressure) the mode of the volume population is observed for a 15 nm pore channel diameter and the relative difference V_{PR} between fractional and total pore volumes indicates that more than 80% of pores have a size smaller than about 200 nm (Table 3). For samples heated at 10°C min^{-1} up to 1180°C, this main pore population peak is shifted from 15 to 50 nm while the V_{PR}, indicates that more than 90% of pores are now smaller than 200 nm. This means that the mean pore size increases but also that no large pores develop during the first densification step associated with the phase transformation. For samples heated at 1°C min^{-1} up to 1180°C the situation is rather different. The pore population is shifted upward towards the 200 nm limit of this method. This is coherent with the V_{PR} which indicates that after the low heating rate cycle, more than 75% of the pore volume fraction corresponds to pores with size larger than about 200 nm. Hg porosimetry was carried out on a limited number of sample and it was found that the results for the green bodies and 10°C min^{-1} runs gave very similar results to the nitrogen adsorption (within 10%). The 1°C min^{-1} runs gave total pore volumes similar to the density measurements with average pore sizes around 100 nm. As these results do not add significantly to the data already presented and are in qualitative agreement with those presented, they were not reported.

For both Batch 1 and Batch 4 powder compacts, various modifications of the heating conditions and sintering temperatures, after a phase transformation performed at 10°C min^{-1} heating rate, were made to try and improve the final densities while conserving a submicron grain size without sintering temperatures higher than 1450°C. For Batch 1 powder compacts the most favourable conditions seem to be 10°C min^{-1} to 1450°C followed by 4 h at 1450°C; after this treatment, the density was 3·35 g cm^{-3} (84·4%) and the grain size 1·7 μm [Fig. 10(a)]. For Batch 4 powder compacts (250 MPa CIP pressure) the best compromise was 10°C min^{-1} up to 1180°C and 1°C min^{-1} from 1180°C to 1450°C; such conditions lead to a final density of 3.71 g cm^{-3} (93·5%) with a grain size of 1 μm [Fig. 10(b)].

These results show the direct influence of the α content, the green density, the heating rate on the densification behaviours of transition alumina powder compacts during the step corresponding to the transformation into the stable α phase and on the subsequent sintering and densification. In the following analysis, interpretation and discussion, we propose some mechanisms to explain these general behaviours.

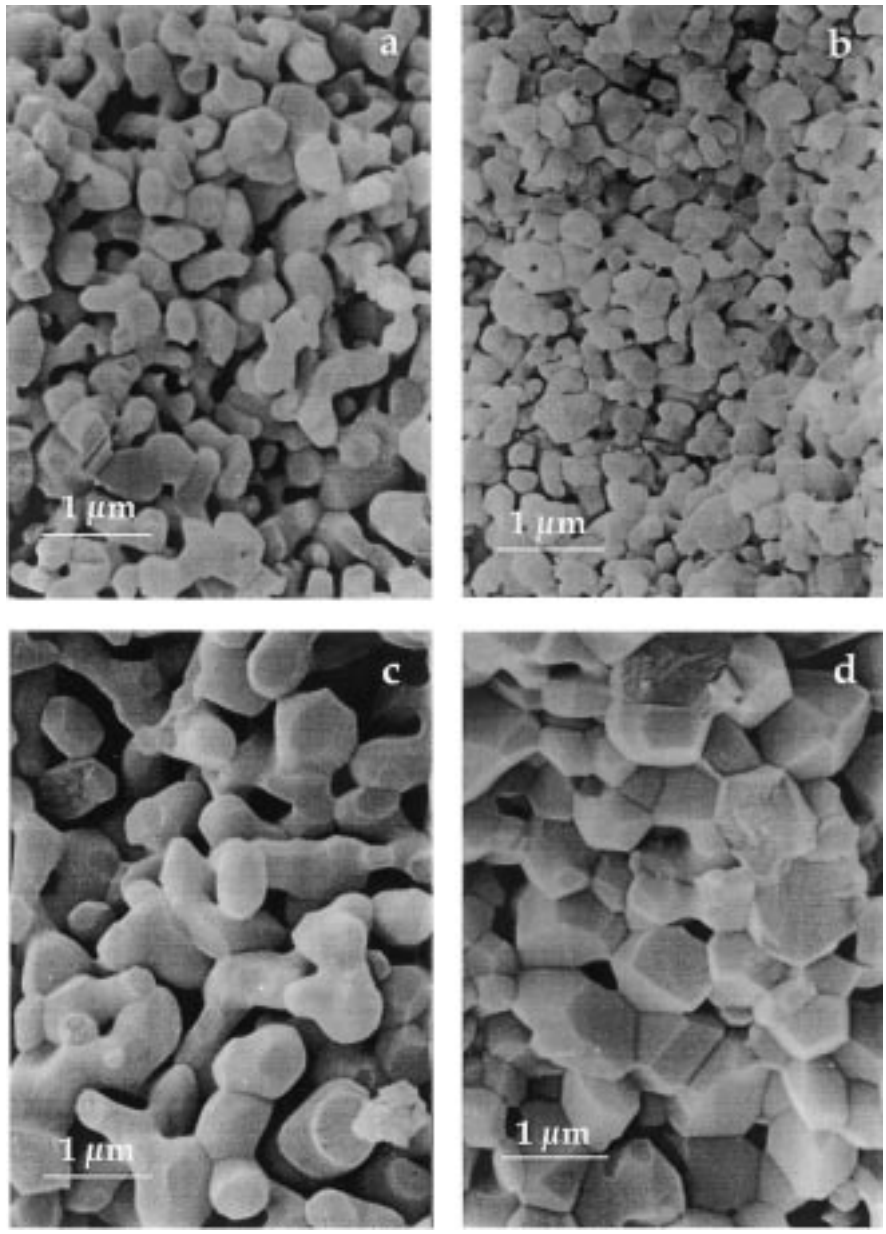

Fig. 7. Microstructures of sintered samples up to 1450°C in constant heating rate conditions: (a) Batch 1: $10°C\,min^{-1}$, $\rho_f = 2{\cdot}37\,g\,cm^{-3}$; (b) batch 4: $10°C\,min^{-1}$, $\rho_f = 2{\cdot}98\,g\,cm^{-3}$; (c) batch 1: $1°C\,min^{-1}$, $\rho_f = 2{\cdot}35\,g\,cm^{-3}$; (d) batch 4: $1°C\,min^{-1}$, $\rho_f = 3{\cdot}61\,g\,cm^{-3}$. All green samples were cold isostatically pressed under 250 MPa.

4 Analysis, Interpretation and Discussion

In this section, we begin by focusing on the first densification step which corresponds to the transformation of transition metastable alumina into the stable α phase.

If we consider only the difference of theoretical density of the two alumina crystalline phases (θ and α), the relative density variation for the transformation $(\Delta\rho_R)_{th}$ should be:

$$(\Delta\rho_R)_{th} = \frac{\rho_\alpha - \rho_\theta}{\rho_\theta} = \frac{3{\cdot}987 - 3{\cdot}6}{3{\cdot}6} = 10{\cdot}75\%$$

This value is much lower than experimental $\Delta\rho_R$s reported in this study. The apparent increase in density during the first densification step cannot be explained simply by the increase of density from $\gamma(\theta)$ to α phase. This does assume the theoretical density of $3{\cdot}6\,g\,cm^{-3}$ is correct for the θ phase but, even if the practical density is as low as $3{\cdot}4\,g\,cm^{-3}$, the $\Delta\rho_R$, would still be 17·25% and still significantly lower than most of the results shown in Fig. 6. Other examples of such unexplained increases of compact density during a phase transformation can be drawn from the literature by reanalysing the data (the data is not always presented in a suitable form to evaluate the $\Delta\rho_R$ easily). Messing[19] published only very recently shrinkage and densification curves of seeded boehmite in a paper devoted to the fabrication of porous alumina ceramics. In this case, the calculated $\Delta\rho_R$ is about 85% for $15°C\,min^{-1}$ heating rates

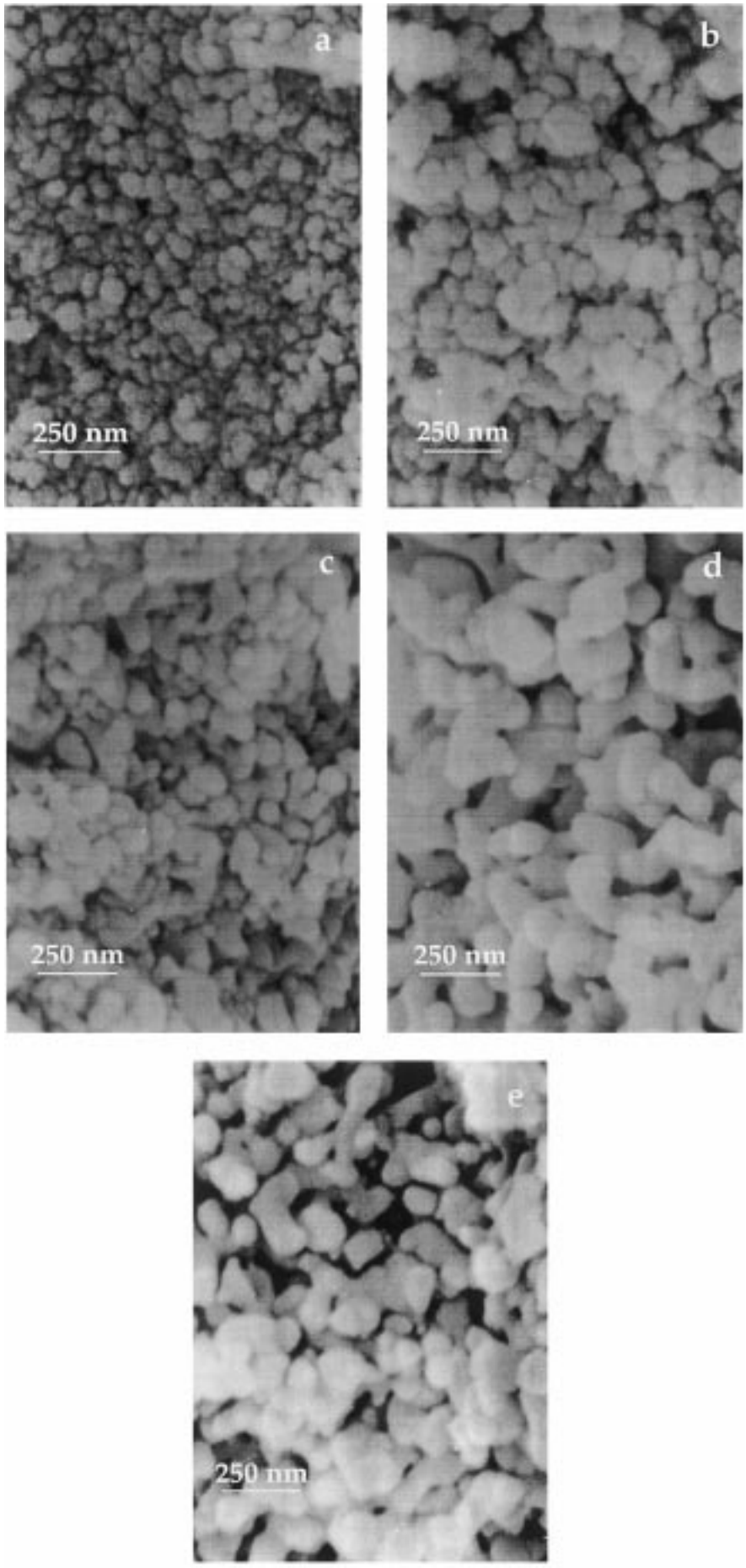

Fig. 8. Microstructures evolution during the first apparent densification step for 250 MPa CIP samples of batch 1 (927 N) and batch 4 [8966 (4 Mg)] powders:(a) typical green microstructure (batch 1), $\rho = 1{\cdot}52\,g\,cm^{-3}$; (b) batch 1 sample heated at $10°C\,min^{-1}$ up to 1180°C, $\rho = 1{\cdot}96\,g\,cm^{-3}$; (c) batch 4 sample heated at $10°C\,min^{-1}$ up to 1180°C, $\rho = 2{\cdot}00\,g\,cm^{-3}$; (d) batch 1 sample heated at $1°C\,min^{-1}$ up to 1180°C, $\rho = 1{\cdot}82\,g\,cm^{-3}$; (e) batch 4 sample heated at $1°C\,min^{-1}$ up to 1180°C, $\rho = 1{\cdot}95\,g\,cm^{-3}$.

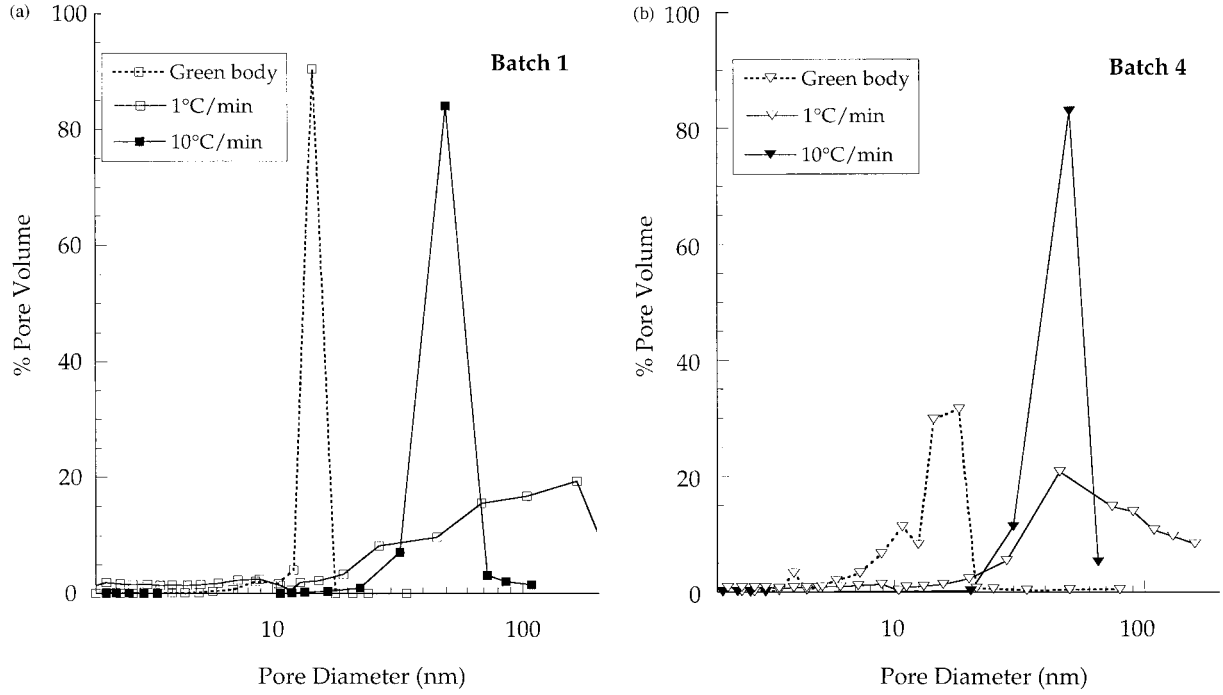

Fig. 9. Pore size distributions in green body and in samples heated up to 1180°C at 10 and 1°C min^{-1}: (a) batch 1 powder samples; (b) batch 4 powder samples.

Table 3. Evolution of pore volume fraction during the first densification regime R1 (up to 1180°C) for two different heating rates

	Batch 1 (927N)			*Batch 4 (8966 (4 Mg))*		
	$V_{PF}{}^{a}$ *(cm^3 g^{-1})*	$V_{PT}{}^{b}$ *(cm^3 g^{-1})*	$V_{PR}{}^{c}$ *(%)*	V_{PF} *(cm^3 g^{-1})*	V_{PT} *(cm^3 g^{-1})*	V_{PR} *(%)*
Green compacts 250 MPa CIP	0·3196	0·378	−15·6	0·360	0·384	−6·2
10°C min^{-1} 1180°C	0·250	0·259	−3·5	0·235	0·249	−5·6
1°C min^{-1} 1180°C	0·003	0·298	−89·9	0·060	0·262	−77·1

[a] V_{PF}, pore volume fraction from N_2 porosimetry.
[b] V_{PT}, pore volume fraction from density (ρ) measurement. $V_{PT} = \frac{1}{\rho} - \frac{1}{\rho_{\theta \text{ or } \alpha}}$ with $\rho_\theta = \theta$ theoretical density = 3·60 g cm^{-3}, $\rho_\alpha = \alpha$ theoretical density = 3·97 g cm^{-3}.
[c] $V_{PR} = \frac{V_{PF} - V_{PT}}{V_{PT}}$, relative fraction of pore volume non detected by nitrogen porosimetry or pores with diameter > 200 nm.

with a density just before the last phase transformation of 1 g cm^{-3}. In papers on titania sintering,[20,21] it was noticed but not discussed in detail that the shrinkage attributed to the transformation of anatase to rutile could not be explained simply by the increase of density from the anatase to rutile phase. In our alumina study, porosimetry measurements, carried out just after the first densification step, reveal pronounced modifications of the pore size distribution depending mainly on the heating rate. This suggests a grain rearrangement process coupled with the phase transformation.

The formation of α-alumina via transition aluminas occurs by a nucleation and growth process during heating. The nucleation step depends on the density of nuclei which can result from:

- the number per unit volume of α grains already present in the green body voluntary or involuntary seeded during the powder processing;
- the number of mechanical contacts between transition alumina particules which are potential nucleation sites;[2] the higher the green density, the higher the number of such sites;
- the heating rate; like for classical metallurgical transformation occuring on cooling, the number of nucleation sites increases with increasing heating rate.

In the case of Batch 1 and Batch 4 powders, we have very roughly estimated the number of nucleation sites for two heating rates (1 and 10°C min^{-1}). We assume that each α grain after the transformation (1180°C) results from a single nucleus, we calculated the nucleation site densities (N_{SD}) initiated in the green bodies from the α-grain sizes at 1180°C and from sample densities before

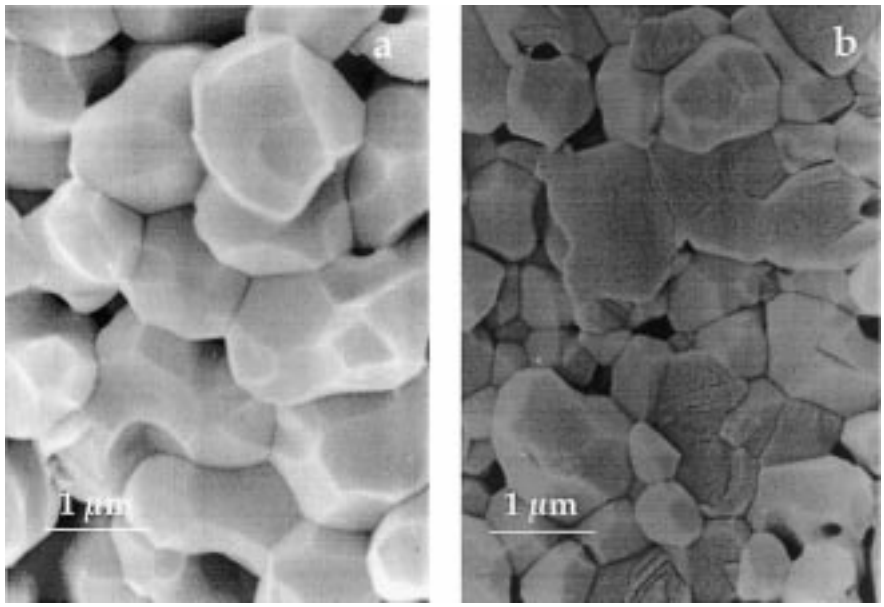

Fig. 10. Microstructures of samples (250 MPa CIP) with improved microstructures and densities with 10°C min^{-1} heating rate up to 1180°C for phase transformation and: (a) 10 from 1180°C min^{-1} up to 1450°C with 4 h at 1450°C, batch 1 powder; (b) 1°C min^{-1} from 1180°C up to 1450°C and cooled without soaking time, batch 4 powder.

and after the transformation. In the case of Batch 1 for example, for 1°C min^{-1} heating rate, the mean α grain size, d_α is 150 nm at 1180°C just after the transformation. The mean volume, V_α, and the mean mass, m_α, of an α grain are, respectively:

$$V_\alpha = \frac{4}{3}\pi\left(\frac{d_\alpha}{2}\right)^3 = 1{\cdot}8\ 10^{-15}\ \text{cm}^3$$

and

$$m_\alpha = \rho_\alpha V_\alpha = 7{\cdot}1\ 10^{-15}\ \text{g}$$

Consequently,

$$N_{SD} = \frac{\rho_0}{m_\alpha} = 2 \times 10^{14}\ \text{cm}^{-3}$$

For 1°C min^{-1}, these estimated N_{SD}s were 2 and 8×10^{14} nuclei cm^{-3} for Batch 1 and Batch 4 powder compacts, respectively, whereas for 10°C min^{-1} the N_{SD}s were estimated to be 10 and 16×10^{14} nuclei cm^{-3} for Batch 1 and Batch 4, respectively (250 MPa CIP pressure). The relative increase of the N_{SD}s due to the faster heating rate is more pronounced for Batch 1 samples (400%) than for Batch 4 (100%) which already contains a significant number of α grains in the green state. McArdle and Messing,[22] in their recent work, have reported seeding boehmite with α-Fe_2O_3 particules with densities of 10^{14} particles cm^{-3} in dried gels with densities much lower than 1 g cm^{-3}; for sintering, their samples were heated at 15°C min^{-1} up to the temperature of a classical isothermal treatment which is higher than that of the transformation. Apart from our much higher green densities, our other experimental data of the same order of magnitude to those of McArdle and Messing's work[22] suggesting our rough calculations are at least reasonable.

Coming back to the effect of heating rate on the transformation relative density changes, $\Delta\rho_R$'s (Fig. 6), it appears that the $\Delta\rho_R$ increases with both the heating rate and the α-content. This suggests that this unexplained amplitude of the $\Delta\rho_R$ depends on the nucleation site densities. When a particle transforms from the θ to α phase, if the neighbouring grains are not close packed or not symmetrically arranged, the crystallographic volume reduction can induce non-symmetrical interparticle forces causing particles or grains to slide and to rotate. Such relative particle movement leads to particle rearrangement, the amplitude of which depends on the free space available and on the density of nucleation sites. Early sintering studies on the initial sintering steps also discussed and predicted rearrangement due to non-symmetrical forces brought about by particle shrinkage and their packing arrangement.[23] Multiplication of local perturbations caused by particle transformation leads to a generalized grain rearrangement and consequently the microstructure evolves toward a more homogeneous one in the course of the transformation. Such a rearrangement process can justify an amplitude of $\Delta\rho_R$ much higher than the simple crystallographic density change [schematically illustrated in Fig. 11(c)]. For identical constant heating rates, samples with lower densities exhibit larger $\Delta\rho_R$s (Fig. 5), this may be because the increase of free space available dominates the decrease of possible nucleation sites related to the lower number of interparticle contacts. The rearrangement of particles may be more active at lower

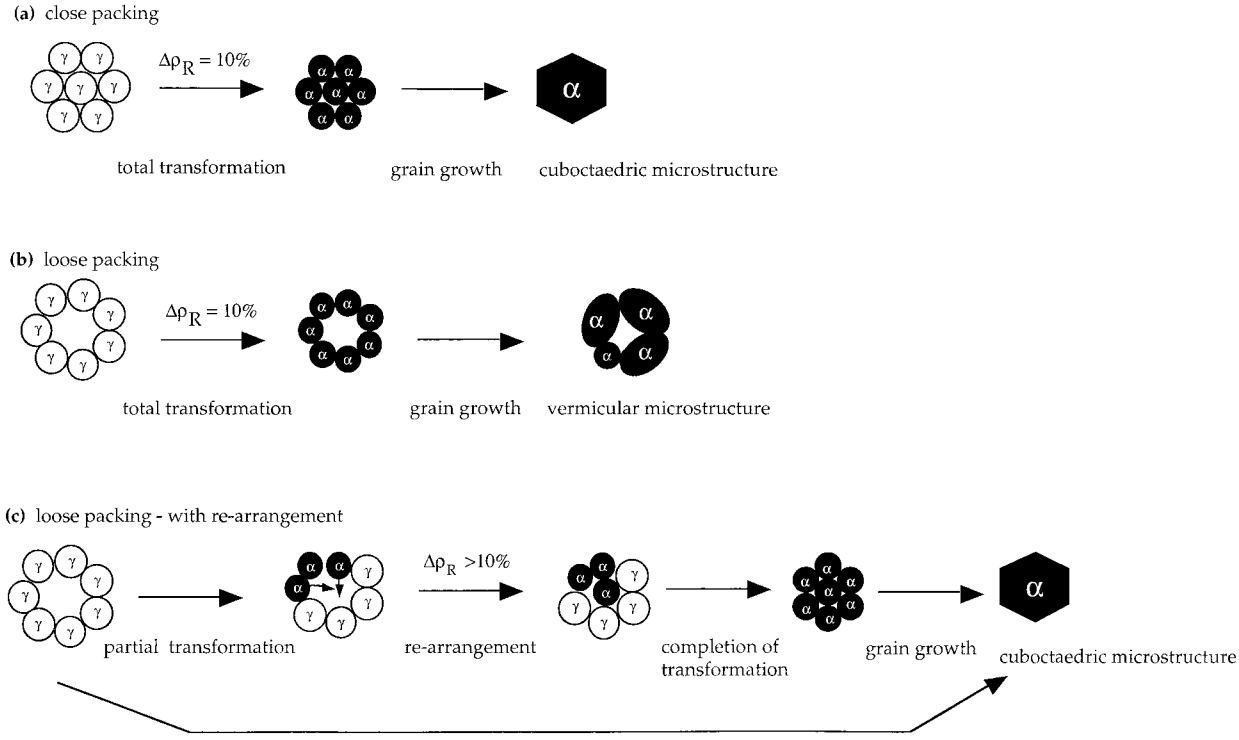

Fig. 11. Schematic transformation induced microstructure modifications (a) transformation and grain growth in green compact close-packing $\Delta\rho_R = 10\%$; (b) nucleation, transformation and grain growth in low density green body $\Delta\rho_R = 10\%$; (c) nucleation, transformation, rearrangement and grain growth in low density green body $\Delta\rho_R > 10\%$.

green density because of the lower hinderance met in a more open particle network. At the other extreme, a sample of close packed monosize particles should exhibit the theoretical $\Delta\rho_R$ [10·75% for θ to α transformation in alumina; Fig. 11(a)].

In the case of very low density samples before the last transformation (θ to α), as for α-seeded sol–gel boehmite derived green bodies, since there is a very large free space available associated with an optimized number density of α grains, one should expect very large $\Delta\rho_R$ as shown above (estimated to be 85%), but which is rarely reported as such.[21] If the transformation is performed during a isothermal treatment, the number of active nucleation sites is likely to be lower than under constant heating rate conditions and so the $\Delta\rho_R$ will also be smaller. This tendancy was confirmed by the low $\Delta\rho_R$, measured during an isothermal treatment at 1040°C (heating rate 10°C min^{-1} up to 1040°C) of a Batch 1 compact (250 MPa CIP pressure): the $\Delta\rho_R$ was 15% which is much lower than the 24% observed for 10°C min^{-1} heating rate (Fig. 5).

Well activated and controlled, such rearrangement mechanisms during a phase transformation from a metastable phase to the stable one, should result in a coordinated repacking, an improved packing density and a homogenization of the microstructure very suitable for the further sintering of fine grained α-aluminas microstructure following the classical mechanisms. The decrease of the second densification rate peak temperature, R2, coupled with an increase of initial α phase content and probably an increase of the $\Delta\rho_R$ (although not clearly shown in this study) would explain an improvement of the sinterability of samples after transformation into α stable phase due to an improved packing density at temperatures before grain growth becomes too important. In recent studies on sintering of fine oxide powders, Chen and Chen[24,25] propose that particle coarsening can also lead to coordinated particle movement and packing-density increase. They concluded that 'very fine, surface-active powders that coarsen rapidly are uniquely capable of taking advantage of coarsening-motivated homogenization and rearrangement densification processes'. Our conclusion is very similar with the transformation process replacing the coarsening process. In the transformation case, a particle coarsening mechanism cannot be excluded and could contribute to the $\Delta\rho_R$ [Fig. 11(c)]; at the end of the transformation (SEM observations on samples heated up to 1180°C) the α grain sizes are somewhat larger than the green particle sizes but here we feel that the phase transformation plays the key role.

There are of course several other factors which have to be taken into account before we arrive at our goal of monolithic nanograined ceramics by pressureless sintering, such as particle or agglomerate packing, the effect and use of dopants and the

interparticle forces involved in the particle rearrangement [interparticle friction, attractive dispersion (van der Waals) forces across air or a glassy phase]. Here the dominant attractive forces for our nanosized powders will be the dispersion or van der Waal forces.

The packing of nanopowders is complicated by the fact that they are invariably made up of agglomerates 10–20 times larger than the primary nanoparticle. One major factor in the densification of nanopowder compacts is to stimulate interagglomerate densification and not to have a predominance of intra-agglomerate densification leaving large stable pores in the final piece[7] as seen with the $1°C\,min^{-1}$ heating rates above. Some attempts in this direction have been made with these Baïkowski powders using a bimodal distribution approach.[26] Bimodal distributions with aggregates of around 1·0 and 0·1 μm were slip cast with the hope that the 0·1 μm aggregates filled the inter-aggregate pores between the 1 μm aggregates. This should lead to a more homogeneous pore size distribution and particle coordination numbers throughout the whole green body, leading thus to a more homogeneous sintering step. This bimodal approach did not prove fruitful, mainly because the coarse particle size distribution was not well adapted but sintered densities of 97% theoretical were achieved from attrition milled Batch 1 type powders. Further work in the light of the rearrangement mechanisms discussed here could prove very fruitful. The dopants, frequently used in the sintering of α-alumina powders may also play an important role in the first densification region before they take on their normal role for the second α sintering region. The proposed particle rearrangement mechanism associated with the phase transformation will be greatly influenced by particle–particle interactions via the particle surface. If dopants modify the composition and hence physical properties of the surface this would have an influence on the inter-particle friction coefficient. by the formation of a glassy phase for example. Also the attractive van der Waals forces between the particles may be influenced by the appearance of a glassy phase and consequently the equilibrium distance between the particles as discussed by Chiang *et al.*[27] for the case of thick-film resistors. If the hinderance to rearrangement could be thus reduced to a minimum, then we may be able to take advantage of even higher heating rates than the $20°C\,min^{-1}$ maximum suggested in Fig. 6. Here the rearrangement was perhaps kinetically limited and the expected increase in nucleation site densities at $30°C\,min^{-1}$ could not significantly increase the relative density change. Such high heating rates could also give rise to thermal gradient problems in centimetre sized samples.

These mechanisms of rearrangement and microstructural homogenization illustrated in this work on transition aluminas should also be applicable to other nanometric oxide powders which are often metastable and incur a phase transformation on sintering.[28–30]

5 Conclusions

Sintering studies of commercial powders which mainly differ by their α-alumina contents have clearly pointed out the influence of several parameters, such as green density, heating rate, α-alumina initial content. on the phase transformation γ–α. An enhanced densification, over and above that expected for the γ (θ) to α phase transition, is clearly observed by plotting relative density changes versus temperature. This enhanced relative density change is brought about particle rearrangement during the transformation, the degree of particle rearrangement being influenced by the above mentioned parameters.

Further studies on the effects of doping elements on the transformation-densification behavior of the same γ-alumina raw powder batch should help us to improve the efficiency of the packing, to lower the temperature of the α sintering regime (R2) and thus to produce α-alumina fine grained materials.

Acknowledgements

The authors are grateful to Mr Droguet (Baïkowski) for providing γ-alumina powders and to undergraduate students (A. Ferrand, C. Kulichenski, F. Herbst) for their experimental contributions.

References

1. Levi, C. G., Metastability and microstructure evolution in the synthesis of inorganics from precursors. *Acta. Mater.*, 1998, **46**, 787–800.
2. Dynis, F. W. and Halloran, J. W., Alpha alumina formation in alum-derived gamma alumina. *J. Am. Ceram. Soc.*, 1982, **65**(9), 442–448.
3. Badkar, P. A. and Bailey, J. E., The mechanism of simultaneous sintering and phase transformation in alumina. *J. Mat. Sci.*, 1976, **11**, 1794–1806.
4. Kumagai, M. and Messing, G., Enhanced densification of boehmite sol–gels by α-alumina seeding. *J. Am. Ceram. Soc.*, 1984, **67**(11), C230–C231.
5. Kumagai, M. and Messing, G., Controlled transformation and sintering of a boehmite sol–gel by α-alumina seeding. *J. Am. Ceram. Soc.*, 1985, **68**(9), 500–505.
6. Messing, G. and Kumagai, M., Low-temperature sintering of α-alumina-seeded boehmite gels. *Am. Ceram. Soc. Bul.*, 1994, **73**, 88–91.
7. Prouzet, E., Fargeot, D. and Baumard, J. F., Sintering of boehmite-derived transition alumina seeded with corundum. *J. Mat. Sci. Let.*, 1990, **9**, 779–781.

8. Matkin, D. I., Munro, W. and Valentine, T. M., The fabrication of α-alumina by reactive hot-pressing. *J. Mater. Sci*., 1971, **6**, 974–980.
9. Ishitobi, Y., Shimada, M. and Koizumi, M., Reactive pressure sintering of alumina. *Am. Ceram. Soc. Bul*., 1980, **59**, 1208–1211.
10. Mishra, R. S., Lesher, C. E. and Mukherjee, A. K., High-pressure sintering of nanocrystalline γ-Al_2O_3. *J. Am. Ceram. Soc*., 1996, **79**, 2989–2992.
11. Nordahl, C. S. and Messing, G., Transformation and densification of nanocrystalline θ-alumina during sinter forging. *J. Am. Ceram. Soc*., 1996, **79**, 3149–3154.
12. Dauzat, M., Pijolat, M. and Soustelle, M., Influence de l'addition de cations sur les transformations successives $\gamma \rightarrow \delta \rightarrow \theta \rightarrow \alpha$ de l'alumine. *J. Chimie Physique*, 1988, **85**(9), 865–869.
13. Tsai, D. S. and Hsieh, C. C., Controlled gelation and sintering of monolithic gels prepared from γ-alumina fume powder. *J. Am. Ceram. Soc*., 1991, **74**(4), 830–836.
14. Xue, L. A. and Chen, I. W., Influence of additives on the γ–to $-\alpha$ transformation of alumina. *J. Mat. Sci. Lett*., 1992, **11**, 443–445.
15. Wu, S. J., De Jonghe, C. and Rahaman, M. N., Sintering of nanophase γ-Al_2O_3 powder. *J. Am. Ceram. Soc*., 1996, **79**(8), 2207–2211.
16. Kumar, K. N. P., Keiser, K., Burggraaf, A. J., Okubo, T., Nagamoto, H. and Morooka, S., Densification of nanostructured titania assisted by a phase transformation. *Nature*, 1992, **358**, 48–51.
17. Legros C, Carry C, *et al*. Phase transformation and sintering of transition alumina powders: effects of zirconium, yttrium and titanium as doping elements. *J. Eur. Ceram. Soc*., in preparation.
18. Levin, I. and Brandon, D., Metastable alumina polymorphs: crystal structures and transition sequences. *J. Am. Ceram. Soc*., 1998, **81**(8), 1995–2012.
19. Kwon, S. and Messing, G. L., Constrained densification in boehmite–alumina mixtures for the fabrication of porous alumina ceramics. *J. Mater. Sci*., 1998, **33**, 913–921.
20. Echeverria L. Effect of rutile on densification of anatase. In *Ceramic Transactions, Ceramic Powder Science III*., Vol. 12, ed. G. L. Messing, S. Hirano and H. Hausner. American Ceramic Society, Westerville, OH, 1990, pp. 649–658.
21. Kim, D. W., Kim, T. G. and Hong, K. S., Origin of shrinkage anomaly in anatase. *J. Am. Ceram. Soc*., 1998, **81**(6), 1692–1694.
22. McArdle, J. L. and Messing, G. L., Transformation, microstructure development, and densification in α-Fe_2O_3-seeded boehmite-derived alumina. *J. Am. Ceram. Soc*., 1993, **76**(1), 214–222.
23. Exner, H. E. *Grundlagen von Sintervorgängen*, ed. G. Petzow, Gebrüder Borntraeger Berlin, Stuttgart, 1978.
24. Chen, P. L. and Chen, I. W., Sintering of fine oxide powders: I—microstructural evolution. *J. Am. Ceram. Soc*., 1996, **79**(12), 3129–3141.
25. Chen, P. L. and Chen, I. W., Sintering of fine oxide powders: II—sintering mechanisms. *J. Am. Ceram. Soc*., 1997, **80**(3), 637–645.
26. Bowen, P., Charvin, O., Hofmann, H., Carry, C. and Herard, C., Processing of nanosized powders — a bimodal slip casting approach. In *Ceramic Processing Science*, eds. G. L. Messing, F. F. Lange and S. Hirano. Ceramic Transactions Volume 83, The Ceramic Society, 1998, pp. 211–218.
27. Chiang, Y.-M., Silvermann, L. A., French, R. H. and Cannon, R. M., Thin glass film between ultrafine conductor particles in thick-film resistors. *J. Am. Ceram. Soc*., 1994, **77**(5), 1143–1152.
28. Kumar, K. P., Growth of rutile crystallites during the initial stage of anatase-to-rutile transformation in pure titania and in titania–alumina nanocomposites. *Scripta Met. et Mater*., 1995, **32**(6)), 873–877.
29. Kondo, M., Funakubo, H., Shinozaki, K. and Mizutani, N., Formability and sinterability of hydrothermally crystallized monodispersed titanium dioxide particles. *J. Ceram. Soc. Jap*., 1995, **103**(6), 552–556.
30. Allen, A. J., Krueger, S., Skandan, G., Long, G. G., Hahn, H., Kerch, H. M., Parker, J. C. and Ali, M. N., Microstructural evolution during the sintering of nanostructured ceramic oxides. *Am. Ceram. Soc*., 1996, **79**(5), 1201–1212.